powders

MDPI

Article

Linking Consistency in Experimental Results to Surface Topography: A Novel Hypothesis on Laser-Ignited Combustion in Random Particle Packings

Xinghan Li [1,2,*], Zehua Zhang [1], Shiquan Lin [1], Meishuang He [1], Qijun Liu [1], Fusheng Liu [1], Wencan Guo [2] and Hongbo Pei [2]

[1] School of Physical Science and Technology, Southwest Jiaotong University, Chengdu 610031, China
[2] National Key Laboratory for Shock Wave and Detonation Physics, Mianyang 621900, China
* Correspondence: lixinghan2107@163.com

Abstract

Laser-ignited particle combustion is critical to energy, aerospace, and defense applications, yet progress in deciphering its physicochemical mechanisms is hindered by poor reproducibility of combustion data from randomly packed samples. Classical theories attribute this inconsistency to variations in bulk packing density. Here, we propose a novel hypothesis that the consistency of the uppermost surface layer topography is the dominant determinant of combustion reproducibility. A two-/three- dimensional discrete element method (DEM) reveals that increasing packing layers markedly reduces surface topography conformity, while gravitational settling maintains bulk packing density near its theoretical maximum. We introduce a constrained droplet method combining multistage sieving, equal-circle packing in a circle theory, and precision droplet deposition. This approach simultaneously yields particles with a narrow size distribution and enables programmable tuning of packing layer counts, producing multilayer particulate packings that accurately reproduce the structural specifications of DEM model. In situ laser ignition diagnostics show that key combustion metrics—including AlO emission spectral profiles, temporal evolution of spectral full width at half maximum (FWHM), ignition delay, and combustion duration—exhibit a rapid decay in consistency with increasing layer count, closely matching the simulated decline in surface topography conformity. These results are attributable to the nanoscale optical penetration depth of the laser, which anchors the nascent reaction front geometry to the pre-combustion surface topography. In contrast, the near-theoretical- maximum bulk packing exerts a less important influence on this interfacial geometry during subsequent propagation. This work also provides a standardized sample preparation protocol, and enables accurate quantification of key combustion parameters that are inaccessible via conventional methods.

Keywords: laser ignition; random packings; surface topography; pore characteristics; discrete element method; constrained droplet method

Check for updates

Academic Editor: Paul F. Luckham

Received: 25 April 2026
Revised: 12 July 2026
Accepted: 30 July 2026
Published: 4 August 2026

Copyright: © 2026 by the authors. Licensee MDPI, Basel, Switzerland. This article is an open access article distributed under the terms and conditions of the Creative Commons Attribution (CC BY) license.

1. Introduction

Particle combustion is a fundamental phenomenon in natural science and engineering, playing a critical role in energy, chemical industry, aerospace, national defense and other fields [1,2]. Deeper research into its underlying mechanisms is essential for enhancing energy utilization efficiency, optimizing chemical production processes, improving

propulsion systems, and advancing the performance of defense-related equipment. As a multidisciplinary problem intersecting chemistry, physics, and materials science, particle combustion is influenced by a range of intrinsic and extrinsic factors. These include particle properties, oxidizer characteristics, atmospheric conditions, physical constraints, and ignition methods [3–5]. Compared with conventional ignition approaches, laser ignition offers distinct advantages such as precise energy delivery, high spatiotemporal resolution, and non-contact operation [6,7]. Furthermore, laser-based processing and laser-ignitable energetic systems demonstrate the utility of localized optical energy delivery in advanced energy materials [8,9]. Owing to these capabilities, laser ignition has emerged as a key technique for elucidating the complex physicochemical mechanisms governing particle combustion.

A major challenge in current studies is the poor reproducibility of experimental results obtained from random particle packings. This sample preparation method, which relies on natural gravitational deposition to form multilayer particle assemblages, typically yields samples with an uncontrolled conical or triangular topography. Although the use of a metal plate to flatten a sample's top surface is a common preparatory step, the minute scale of the gram-level sample poses a major challenge for quantitatively evaluating its effects. The random packing method has been widely used for its operational simplicity, but it often leads to significant inconsistencies—such as variations in flame spectra and in illumination intensity exceeding 50% between experimental replicates. This high level of deviation fundamentally hinders deeper investigation into the underlying physicochemical mechanisms of the combustion process.

Previous studies have established that particle-size distribution and packing density affect powder-bed structure, ignition, and combustion propagation. Kamaraj et al. [10] quantified particle-size and compact-density effects in Ni-Al powder mixtures, while Averardi et al. [11] reviewed the influence of particle-size distribution on powder-bed packing. Yan et al. [12] reported charge-density-dependent laser-ignition delay and greater experimental scatter at lower charge density in Zr/KClO4. Saceleanu et al. [13] compared laser-ignited Al/CuO nanothermites prepared at different packing densities. Pantoya et al. [14] demonstrated density-dependent reaction propagation in nanothermites and micron thermites. Bharat and Mishra [15] showed that spatial disorder can destabilize or quench heterogeneous combustion fronts, and Sundaram and Yang [16] analyzed packing-density effects on flame propagation in nickel-coated aluminum. Sullivan et al. [17] directly observed rapid reactive sintering that changes constituent morphology during nanothermite combustion, while Stacy and Pantoya [18] investigated laser ignition of loose nanocomposite powders. Collectively, these studies identify packing density and particle organization as important variables, but they do not establish that density variation alone governs run-to-run reproducibility in randomly packed aluminum samples under localized laser heating.

While the prevailing consensus attributes experimental variability under spatially uniform heating to packing density, the relevance of this factor under laser-ignition conditions—characterized by localized energy concentration and a limited penetration depth—remains an open question. We propose that the similarity of surface layer topography may play a decisive role in governing experimental reproducibility in laser-induced combustion. Given the nanoscale optical absorption depth of near-infrared radiation in aluminum [19], the initial optical energy deposition is strongly localized at exposed particle surfaces. Among all particle layers, the surface layer exhibits the greatest morphological deviation due to its highest degree of structural freedom. Consequently, deviations in surface topography can evolve over time during combustion, ultimately leading to significant disparities in observed combustion phenomena. However, classical methodologies often overlook the influence of surface topography, pri-

marily on the basis that surface particles constitute only a minimal fraction of the entire packed sample.

To uncover the dominant factor controlling experimental reproducibility in laser ignition, we examined the influence mechanisms of packing density, surface topography, and pore characteristics on combustion consistency via a combined methodology of numerical simulation, precision sample fabrication, and experimental validation. This research provides an insightful conclusion that offers a deeper mechanistic understanding of the laser-ignition process.

2. Numerical Reconstruction of Packing Structures

2.1. Model

To overcome the challenge of in situ topographic characterization of microscale packed samples, we employed a two-dimensional (2D) and three-dimensional (3D) discrete element method (DEM) to simulate random particle packing. Repeated sampling and statistical analysis enabled systematic interrogation of how surface topography conformity and bulk packing density evolve with increasing layer count.

The DEM model simulates the free fall and gravitational settling of spherical particles within a rigid cylindrical boundary, with randomized initial particle positions replicating the stochasticity of physical sample preparation. Particle motion follows Newton's second law:

$$m_i \frac{d\vec{v}_i}{dt} = \sum \vec{F}_i \tag{1}$$

where m_i is the mass of particle i, $\vec{v}_i$ is the velocity vector of particle i. $\sum \vec{F}_i$ is the vector sum of all external forces acting on particle i, which is mainly composed of gravity, force between particle i and other particles ($\vec{F}_{ix}$), and force between particle i and rigid boundary ($\vec{F}_{ib}$):

$$\sum \vec{F}_i = m_i \vec{g} + \sum \vec{F}_{ix} + \vec{F}_{ib} \tag{2}$$

where $\vec{g}$ is the acceleration of gravity. The interactions between particle i and other particles or rigid boundaries were modeled using a classical rigid-body perfect collision model [20] coupled with a damping model. The impulse in the direction of collision (J_i) is given by:

$$J_i = \frac{-(2+e)\vec{v}_i}{\frac{1}{m_i} + \frac{1}{M}} \tag{3}$$

where M is the mass of the colliding particle or boundary, e is the damping intensity (e = 0 corresponds to perfectly elastic collisions). Subsequent parametric studies confirm that varying e across the range of 0–1 induces <2% variation in key packing metrics. To accelerate numerical convergence while preserving physical fidelity, we adopt e = 0.4. The Velocity Verlet algorithm—a symplectic integrator with second-order accuracy in both position and velocity—is used for numerical time stepping, ensuring long-term energy stability.

To avoid the formation of poorly controlled and characterized topographies that result from unrestricted particle accumulation on a flat plate, we conducted numerical simulations of regular multilayer samples that closely mimic the actual preparation process. Experiments were planned to prepare samples within the inner cavity of a zirconia substrate measuring 2.5 mm in diameter and 2 mm in height. Fully occupying a 2.5 mm diameter circular domain requires approximately 56,600 spheres of 10 μm diameter, rendering a full-scale simulation computationally prohibitive. To circumvent this, we designed a rigid constraint boundary of 2.5 mm in width to conduct both 2D and 3D simulations. The 2D

simulations preserved the full radial particle count (250 particles per monolayer) to capture edge effects, encompassing packings with 1–50 layers. These simulations yielded cross-sectional particle arrangements along the cylindrical axis. Conversely, 3D simulations were executed at two scales: a small-scale model (50 particles/layer) and a large-scale model (770 particles/layer), focusing on 1–5 packing layers to resolve stereoscopic packing structures. To ensure statistical reliability, the 2D simulation condition was repeated five times and the 3D simulation condition was repeated three times. The representative packing configurations for 1–4 layers obtained from the 2D and 3D large-scale simulations are presented in Figures 1 and 2, respectively. Across both 2D and 3D simulations, Figures 1 and 2 consistently demonstrate that the variability in surface topography conformity increases markedly with rising packing layer count.

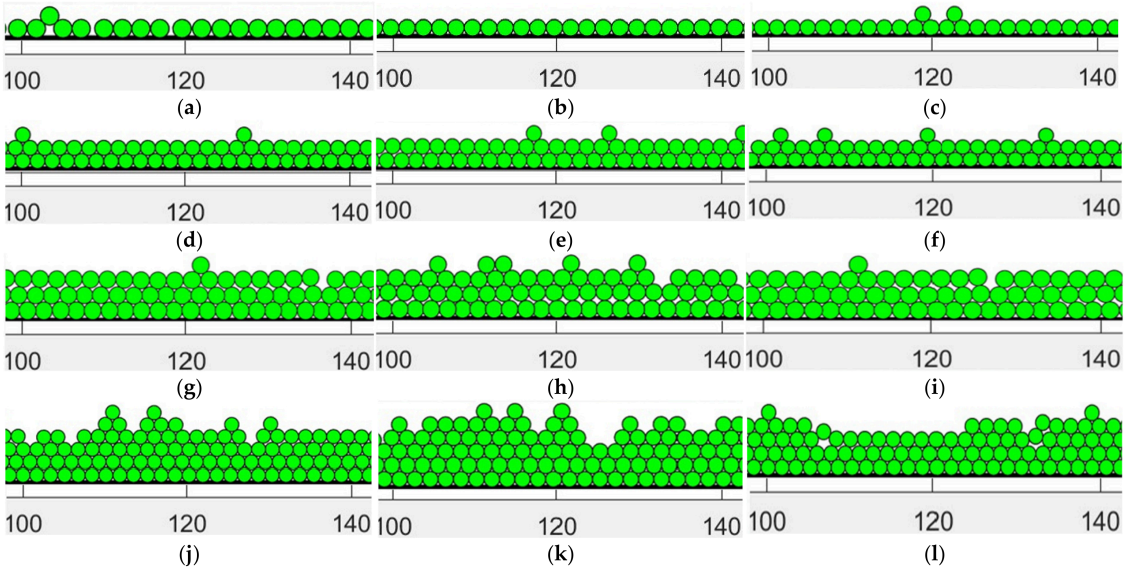


Figure 1. Calculated 2D particle arrangements of three independent trials at the midpoint of the packed samples for layer counts of 1 to 4, and the horizontal axis is scaled in units of 10 μm. Panels (**a**–**c**) correspond to samples with 1 packing layer. Panels (**d**–**f**) correspond to samples with 2 packing layers. Panels (**g**–**i**) correspond to samples with 3 packing layers. Panels (**j**–**l**) correspond to samples with 4 packing layers.

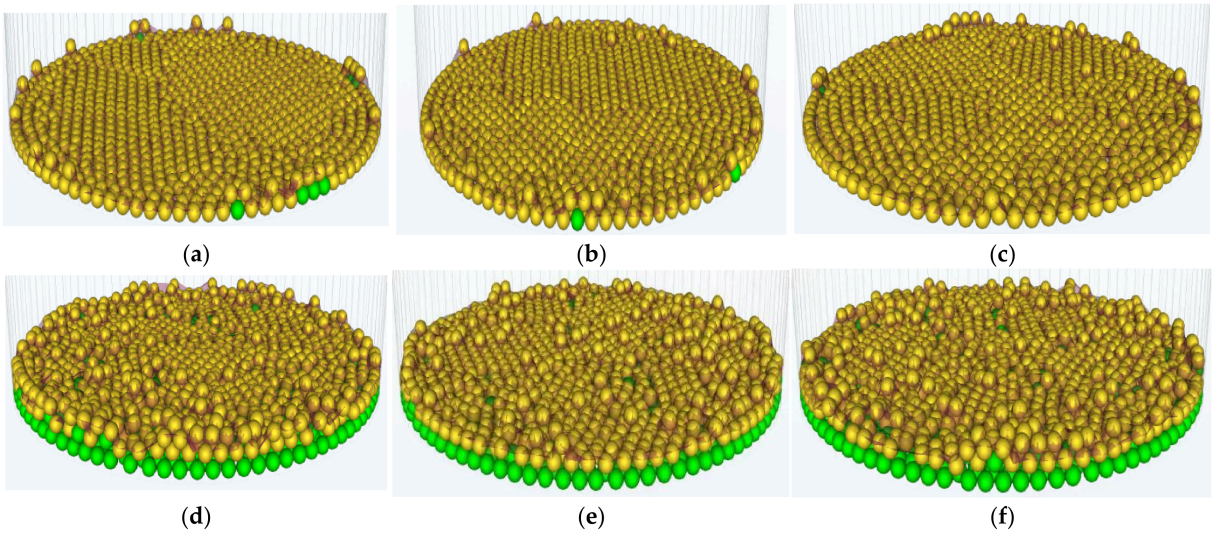


Figure 2. *Cont.*

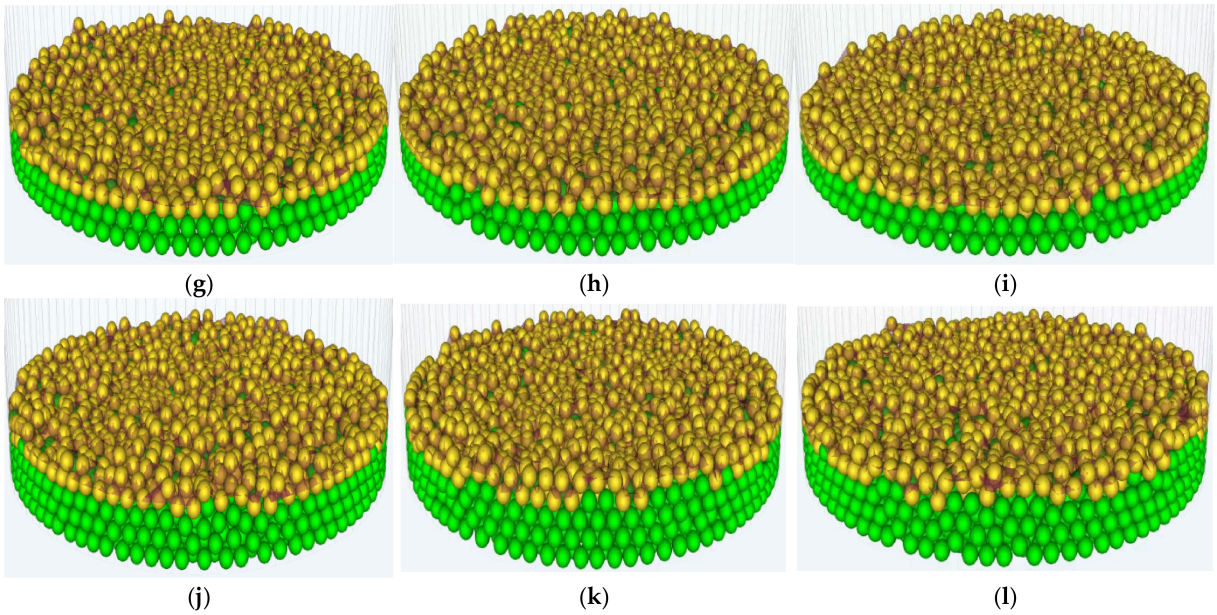


Figure 2. Calculated 3D (large-scale) particle arrangements of three independent trials for layer counts of 1 to 4. The surface particles are highlighted in yellow, while the others are green. Panels (**a**–**c**) correspond to samples with 1 packing layer. Panels (**d**–**f**) correspond to samples with 2 packing layers. Panels (**g**–**i**) correspond to samples with 3 packing layers. Panels (**j**–**l**) correspond to samples with 4 packing layers.

2.2. Function

To quantify surface topography conformity, we define a similarity function S for each trial relative to a reference packing. For 2D simulations, S is derived from the curvature discrepancy between pairs of surface topography curves (discrete polylines defined by the sequential linkage of surface-particle centroids), where S is defined as [21]:

$$S_i = e^{-\left|\frac{d^2 f_i(x)}{dx^2} - \frac{d^2 f_0(x)}{dx^2}\right|} \text{ (2D)} \tag{4}$$

where f represents the surface topography curve of the i-th trial, f_0 is the reference curve selected from the multiple calculation runs, and x is the abscissa. $S = 1$ indicates perfect topographic agreement, while $S = 0$ indicates complete dissimilarity.

For 3D simulations, we extend this framework using a weighted exponential decay function that integrates three orthogonal topographic metrics:

$$S = \exp(-0.60\,E_{\text{height}} - 0.25E_{normal} - 0.15E_{P95}) \text{ (3D)} \tag{5}$$

where E_{height} quantifies vertical height deviation between surfaces [22], E_{normal} captures local normal-vector misalignment after surface registration [23], and E_{P95} describes the 95th-percentile extreme deviation as a robust point-set distance [24]. An exponential decay function is used to transform the aggregated error metric into a normalized similarity score $S \in [0, 1]$.

Bulk packing density is quantified via the filling factor F, defined separately for 2D and 3D simulations:

$$F_i = \frac{N_i \pi R_p^2}{A_i} \text{ (2D)} \tag{6}$$

$$F_i = \frac{N_i 4\pi R_p^3}{3V_i} \text{ (3D)} \tag{7}$$

where N is the total particle count, R_P is the particle radius, A is the 2D packing area, and V is the 3D packing volume. Packing area is defined by two linear edges—a 2 mm sidewall and a 2.5 mm base—culminating in a surface profile at the apex. Packing volume comprises a cylindrical sidewall (diameter: 2.5 mm, height: 2 mm) and a circular base (diameter: 2 mm), with its apex also terminating in a surface profile. In both geometries, the bounding contour is mathematically defined by the convex hull constructed from the centroids of the outermost particles residing along the sample periphery. F is directly proportional to the overall packing density, and $F = 1$ corresponds to an ideal, void-free packing. For close-packed structures, F exhibits theoretically constrained minima F_{dense_min}, which is approximately 0.89 for 2D square packing (derived from the inscribed-circle model within a square lattice) and 0.74 for 3D face-centered cubic (FCC) packing.

2.3. Computational Results

First, we establish the insensitivity of packing characteristics to the coefficient e via 3D DEM simulations, as presented in Figure 3. Across the full physically relevant range of $e \in [0, 1]$ (sampled at 0.1 intervals), the relative deviations in both F and S remain consistently within 1–2% for all tested packing layer counts. These results confirm that e exerts negligible influence on simulated packing structures, justifying the selection of $e = 0.4$ to accelerate numerical convergence without compromising physical fidelity.

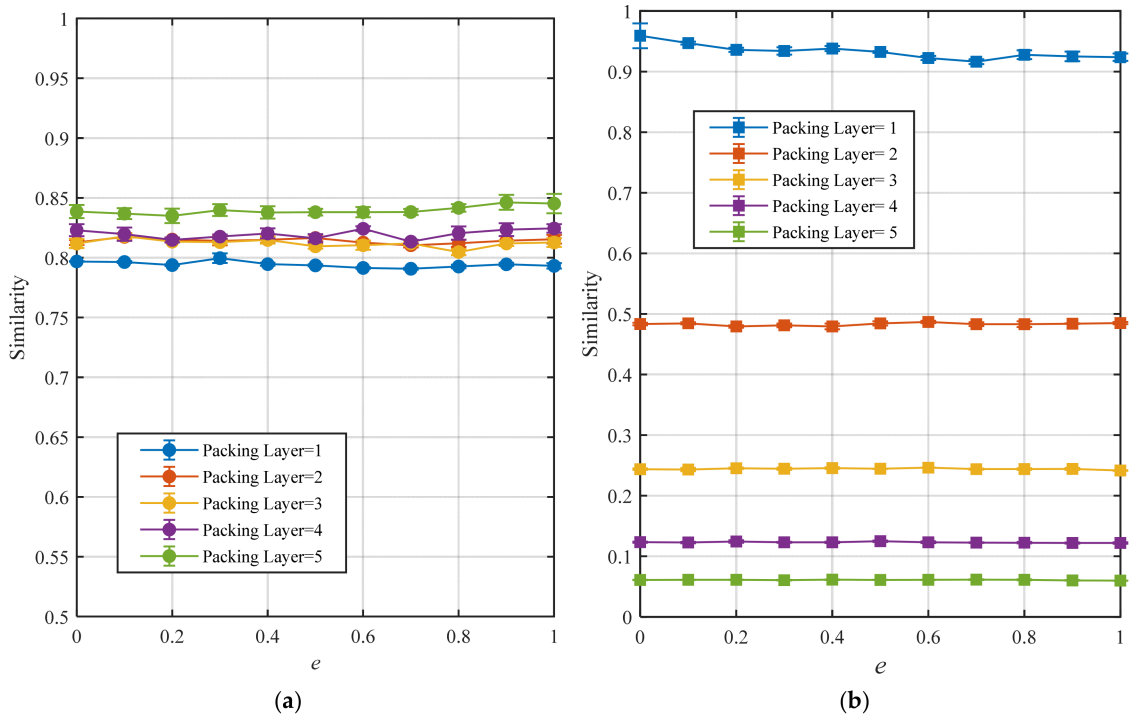


Figure 3. Independence of 3D large-scale packing metrics on the coefficient e. (**a**) Filling factor F and (**b**) surface similarity S.

Figure 4 summarizes the calculated bulk filling factor and surface topography similarity across varying packing layer counts. Notably, despite discrepancies in simulation dimensionality (2D vs. 3D) and particle count per layer, F and S exhibit consistent evolutionary trends with increasing layer number across all model configurations. Two key conclusions emerge from these results.

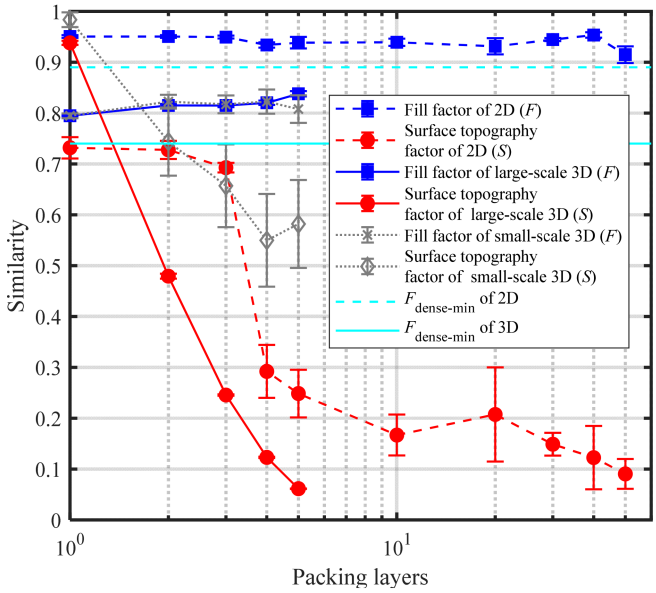


Figure 4. Dependence of surface topography similarity and fill factor similarity on the number of packing layers.

1. Gravitational settling drives consistently dense packing across all models. Our simulation results show that F consistently exceeds F_{dense_min} by 6–12% across all model types, indicating that gravity compels particles into a dense random-close-packed state. For 2D simulations, F remains nearly invariant with increasing layer count. In 3D large-scale simulations, F increases monotonically with layer number, while 3D small-scale simulations show a rise in F from 1 to 4 layers followed by a marginal drop at the 5th layer—a fluctuation attributable to finite-size statistical noise in small particle ensembles. This trend confirms that larger particle counts enhance the robustness and statistical significance of observed packing behavior.
2. Surface topography similarity decays rapidly with increasing layer count. In 2D simulations, S retains a high value (>0.7) for the first three layers before dropping sharply to ~0.2 for four or more layers. 3D small-scale simulations exhibit a quasi-linear decay in S from 0.98 to 0.55 across the first four layers, after which it stabilizes. By contrast, 3D large-scale simulations show a more pronounced quasi-linear decay in S from 0.95 to 0.05 over the first five layers. These results demonstrate that S is sensitive to both simulation dimensionality and particle ensemble size.

Given that the 3D large-scale model most closely approximates the experimental system in terms of dimensionality and particle count, we identify it as the highest-fidelity framework for predicting packing behavior. Three lines of evidence further validate the superiority of the 3D large-scale model. First, the error bars of both S and F do not broaden with increasing layer count, indicating minimal statistical noise. Second, S and F exhibit monotonic evolutionary trends in this framework, whereas other model configurations show spurious non-monotonic fluctuations lacking physical basis. Third, the trends predicted by the 3D large-scale model are quantitatively validated by our experimental measurements. All subsequent statistical analyses in this work are therefore based exclusively on results from the 3D large-scale simulation framework.

3. Sample Preparation

We developed a constrained droplet method to fabricate regular multilayer packings that match computational model specifications, enabling precise control over particle size distribution and layer count (Figure 5). The preparation begins with multistage

classification using stacked test sieves to obtain particles with a narrow, well-defined size distribution near 10 μm, matching the DEM input. The total number of particles is then determined using equal-circle packing in a circle (ECPC) theory [25]. Subsequently, a particle/ethanol suspension with a calibrated concentration was prepared and subjected to 30 min of ultrasonication in a 120 W, 40 kHz water bath with a hermetically sealed vessel. This protocol ensures homogeneous dispersion while effectively suppressing solvent evaporation. Crucially, this ultrasonication regimen induces negligible variation in either particle concentration or the primary particle-size distribution (PSD), consistent with established protocols in prior reports [26,27]. A defined volume of the homogeneous suspension was deposited into the inner cavity of a zirconia substrate using a micropipette. A highly ordered monolayer forms via the facilitated self-assembly of aluminum particles under the combined effects of surface tension and gravity. Samples with packing layers of 1, 2, 3, 4, 5, 10, 20, 30, 40, and 50 were fabricated with five replicates each. Laser ignition experiments were then conducted on all samples under consistent conditions.

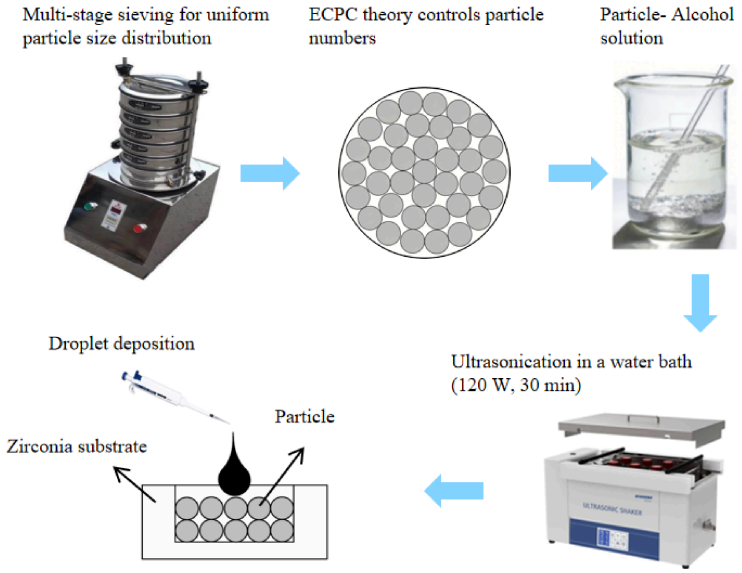
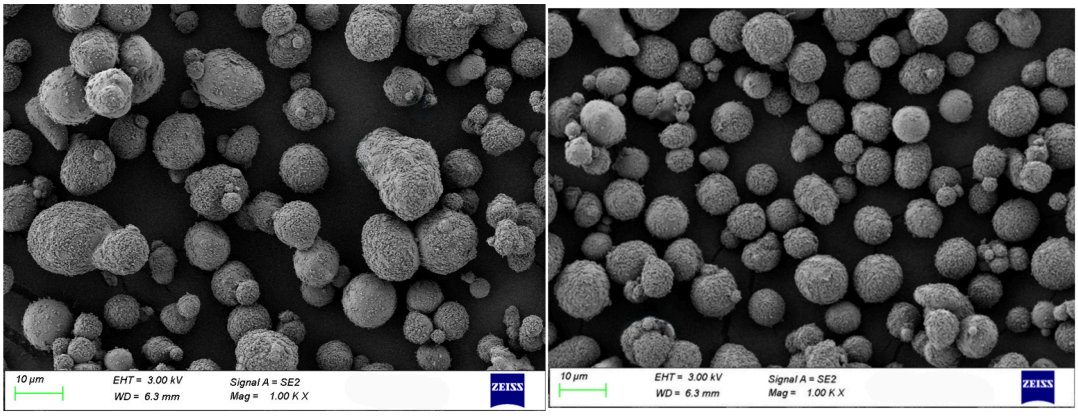


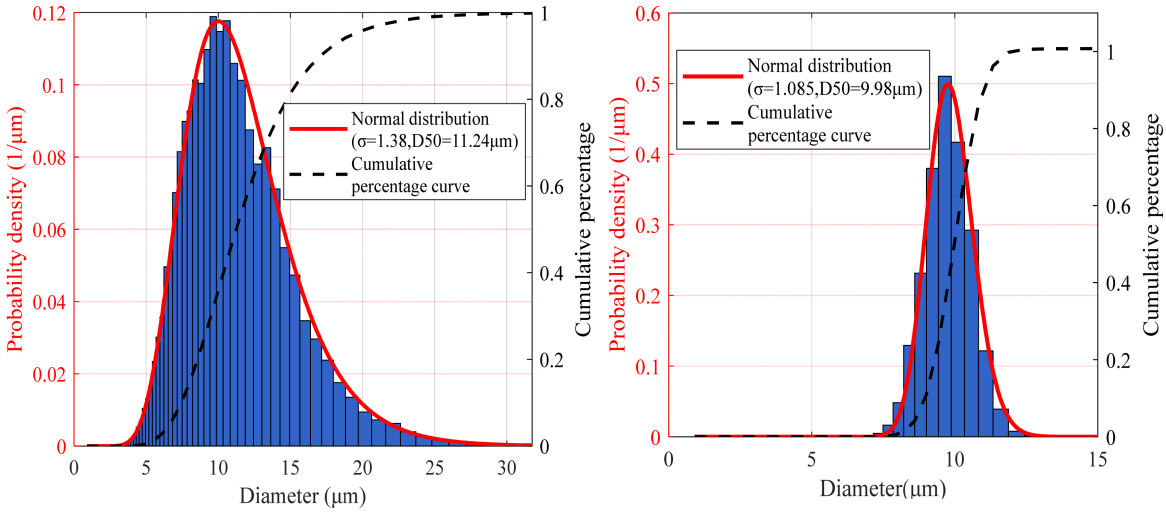
Figure 5. Constrained droplet sample preparation process.

To ensure consistency between the packing arrangement of experimental samples and computational models, careful control of particle shape and size is essential. Aluminum particles were selected as the fuel material due to their well-established use in combustion research. The raw aluminum powder, supplied by Henan Yuanyang Powder Technology Co., Ltd. (Yuanyang, China), exhibited a high degree of sphericity in the scanning electron microscopy (SEM) image (Figure 6a), consistent with the spherical-particle assumption used in the DEM model. The volume-based PSD, shown in Figure 7a, was measured by dry laser diffraction using a Malvern analyzer and the Mie optical model. The raw powder exhibits a broad normal distribution, with a mode diameter of 10 μm and $D10$, $D50$ and $D90$ values of 7.43 μm, 11.24 μm, and 17.16 μm, respectively. Published measurements indicate that aluminum particles near 10 μm lie in a transition regime in which burn time (t) follows $t \propto D_P^{0.7\sim1.15}$ [28], where D_P is particle diameter. Using E-index = 1 as a conservative estimate, the $D10$–$D90$ interval of the raw powder corresponds to a burn-time ratio of 2.31 (0.661–1.527 relative to $D50$). To minimize this confounding effect, multistage sieving with graded test sieves was used to remove the coarse and fine tails of the raw powder.



(**a**) (**b**)

Figure 6. SEM images of aluminum particles: (**a**) before sieving; (**b**) after sieving.



(**a**) (**b**)

Figure 7. Particle size distribution curve: (**a**) before sieving; (**b**) after sieving.

Post-sieving characterization confirmed the efficacy of the multistage sieving protocol: SEM imaging (Figure 6b) revealed improved size uniformity, and particle-size analysis (Figure 7b) exhibited a narrow, unimodal distribution with a mode diameter of 9.76 µm and *D*10, *D*50 and *D*90 values of 8.95, 9.98, and 11.02 µm, respectively. Using the same E-index = 1 estimate, the post-sieving *D*10–*D*90 interval gives a burn-time ratio of 1.23 (0.897–1.104 relative to *D*50), compared with 2.31 for the raw powder. This scaling estimates only the particle-scale contribution of the measured PSD and does not directly predict the duration of the collective packed-bed combustion event. Control experiments using unsieved raw powder further showed that a broad PSD increased the scatter in combustion duration and produced stochastic weak/strong combustion stages. These results establish pre-sieving as an important prerequisite for isolating packing-structure effects on combustion reproducibility.

Precise control over the number of layers in a packed sample requires careful design of the total number of particles, the core of which lies in determining the theoretical number of particles contained in a single layer. The ECPC theory provides an optimal solution to this problem. As a classical mathematical approach to two-dimensional dense packing, this theory yields the densest possible arrangement of identical particles within a larger circle without overlap. For a circle with an diameter of 2.5 mm and aluminum particles with a mode diameter of 9.76 µm, the maximum number of particles accommodable in a

single layer, 56,600, can be derived from this packing theory. The total number of particles required is then calculated as 56,600 multiplied by the number of packing layers. Based on this total, an aluminum/alcohol suspension with an appropriate concentration is prepared to supply the raw material for the constrained droplet sample preparation method.

Sintered dense zirconia was selected as the substrate due to its low thermal conductivity and high density, which collectively provide a consistent thermal environment for combustion experiments. Through hot-press sintering, zirconia achieves high densification (exceeding 95% of theoretical density), minimizing pores and defects to ensure uniform heat transfer. The suitability of zirconia substrates for laser-induced ignition experiments with aluminum particles has been demonstrated in previous work [29].

4. Laser Ignition Experiments

4.1. Results for Sieved Powders

In situ flame radiation spectra were diagnosed using a laser ignition platform to reveal the determinants of experimental consistency, with the system diagram shown in Figure 8. The system comprises three main modules: a laser ignition unit, a spectral diagnosis unit, and a central signal generator for synchronization. A 980 nm semiconductor laser, coupled with a beam expander, constitutes the ignition source, producing a 3 mm diameter spot to ensure full coverage of the 2.5 mm diameter sample. For diagnostics, an optical fiber collects flame emission spectra and transmits them to a spectrometer. The relative positions of the sample and optical fiber were maintained constant across all experiments to enable quantitative spectral comparison. Synchronization of the laser and spectrometer was achieved by the signal generator, ensuring precise timing control. All experiments were conducted at room temperature and atmospheric pressure, with the laser operating at 200 W for 1.5 s. The spectrometer was configured with a 3 ms sampling interval and a 100 μs exposure time.

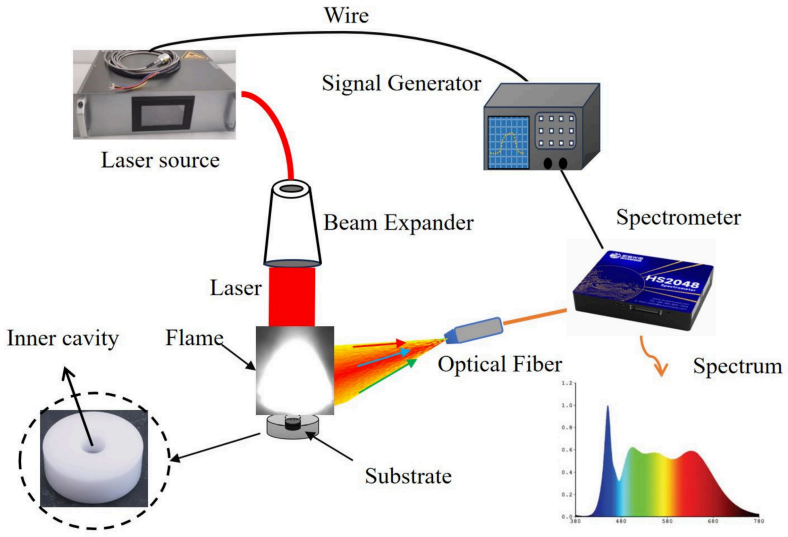


Figure 8. The schematic diagram of laser ignition system.

Laser ignition tests were conducted on samples with packing layers ranging from 1 to 50, with each configuration replicated five times. The combustion process was monitored by tracking the AlO radical's radiation band within the 464.4~513.3 nm wavelength range, a well-established diagnostic signature for aluminum combustion [30]. For direct comparison with the computational results, which were simulated for 1 to 4 layers, the spectral data presented in Figure 9 are limited to this corresponding range.

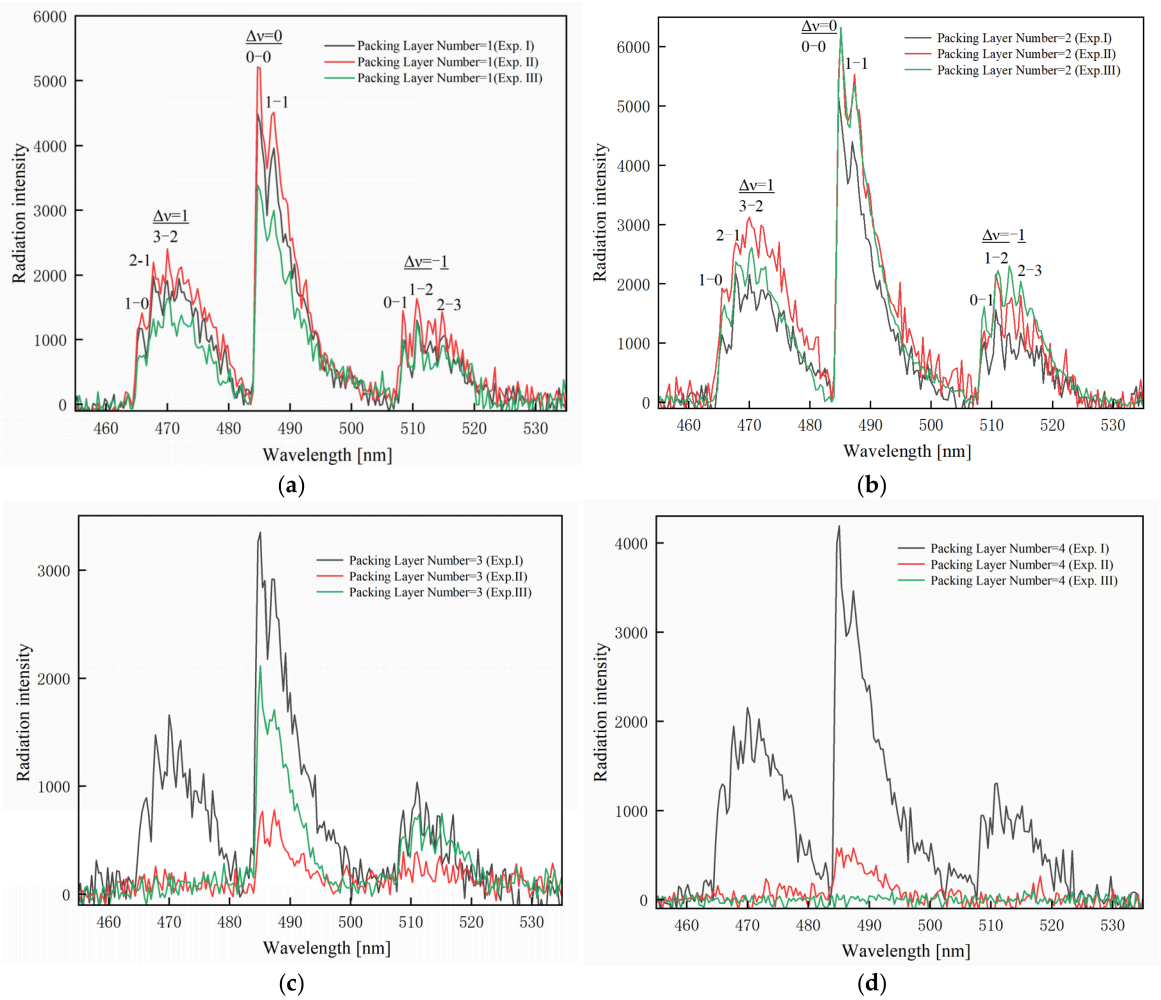


Figure 9. Spectral profiles of the AlO radical emission band (464.4–513.3 nm) recorded at 100 ms without intensity correction, where Δv denotes the net change in the vibrational quantum number, while the v′–v″ notation indicates a specific vibronic transition between defined vibrational energy levels. Results from three independent experimental trials for samples with (**a**) 1, (**b**) 2, (**c**) 3, and (**d**) 4 packing layers.

Figure 9 shows the characteristic spectrum of the AlO radical, and the principal transition bands agree with the reported band assignments [30]. At a fixed time, spectral reproducibility decreases with increasing packing-layer count, broadly following the decrease in surface-topography similarity. Because absolute emission intensity is sensitive to collection geometry and instrument response, the full width at half maximum (FWHM) of a selected band was used as a shape-based spectral descriptor [31]. The Δv = 0 band, particularly the 0–0 transition, was selected because it had the highest signal intensity in the present measurements. Tracking its FWHM through time produces the "AlO characteristic FWHM curve." The curve-similarity function defined above was then used to quantify agreement among replicate FWHM trajectories; the results are shown in Figure 10.

Figure 10 illustrates a rapid decline in the consistency of the AlO characteristic spectral FWHM curve as the number of packing layers increases—a trend that closely mirrors the variation in surface topography consistency. This correlation suggests that the uniformity of the surface layer predominantly governs the spectral consistency of AlO emission. When the stacking layer number is 1 or 2, the similarity function of the AlO spectrum remains above 0.85, accompanied by minimal error bars. In contrast, as the layer count exceeds 3, the similarity drops sharply to 0.1–0.4, while the error bars expand significantly, often

exceeding 50% of the mean value. Notably, the AlO spectral consistency shows a distinct degradation threshold at 3 layers—one layer fewer than the corresponding threshold for surface topography consistency (4 layers). This discrepancy may be attributed to the fact that the two-dimensional computational model underestimates the actual three-dimensional packing consistency, particularly in capturing the increased morphological complexity and fluctuation introduced by additional dimension.

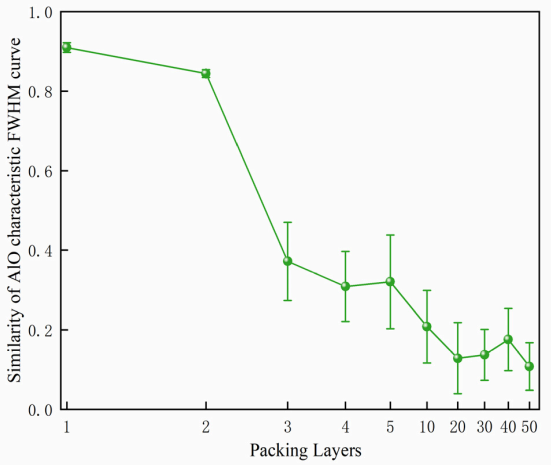


Figure 10. Dependence of AlO characteristic FWHM curve similarity on the number of packing layers.

In combustion diagnostics using emission spectroscopy, the AlO characteristic peak intensity serves as a key factor for determining the ignition delay and combustion duration of samples. It has been widely observed that the AlO characteristic peak exhibits two distinct high-intensity regions: the first region appears within a narrow timeframe, while the second persists for a significantly longer duration [32]. The ignition delay is defined as the interval from the laser ignition point to the peak intensity of the first high-intensity region. The combustion duration is measured as the time interval between the 50% rise point and the 50% fall point of the second high-intensity region. The consistency of the experimentally determined ignition delay and combustion duration, as functions of packing layers, is presented in Figures 11 and 12, respectively.

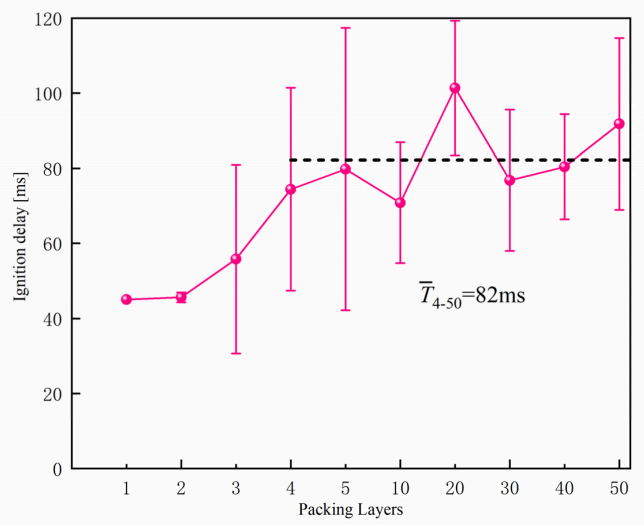


Figure 11. Dependence of ignition delay similarity on the number of packing layers. Dashed line is the average value of the ignition delay.

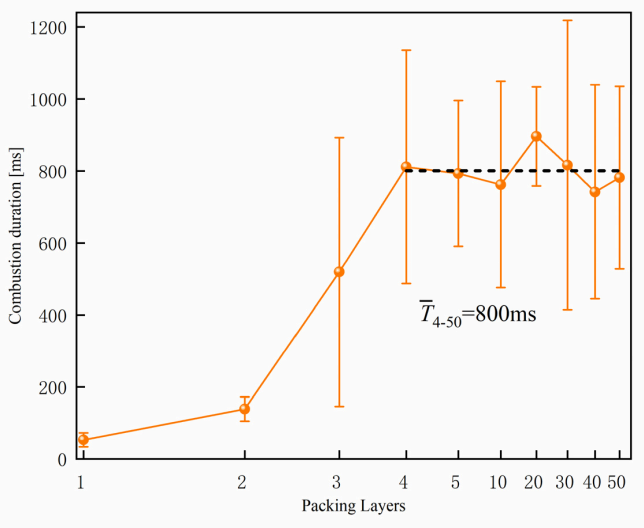


Figure 12. Dependence of combustion duration similarity on the number of packing layers. Dashed line is the average value of the combustion duration.

As shown in Figures 11 and 12, the consistency of both ignition delay and combustion duration decreases rapidly with an increasing number of packing layers—a trend that closely mirrors the decline in surface topography conformity. Quantitatively, samples with 1 and 2 packing layers exhibit excellent experimental reproducibility, as reflected by small error bars in ignition delay (less than 4%) and combustion duration (less than 21%). However, a marked deterioration in consistency occurs when the number of layers exceeds 3. For packs ranging from 3 to 50 layers, the maximum scatter in ignition delay stabilizes in the range of 25–50%, while that for combustion duration remains between 40% and 70%. Such significant data dispersion substantially undermines the reliability and analytical utility of the measured parameters, a phenomenon commonly encountered in randomly packed samples. It should be emphasized that these findings are established within the specific context of laser ignition. Whether surface topography consistency remains the dominant factor under other heating regimes warrants further investigation.

The study further demonstrated that the constrained droplet method enables the measurement of key combustion parameters—such as the upper limits of average ignition delay and combustion duration, as well as the maximum penetration distance of heat flux—which are difficult to obtain using conventional random packing techniques. The observed trend—where the average ignition delay and average combustion duration increase initially and then plateau with additional packing layers under stable heating—is attributed to the heat transfer dynamics within the pack. For non-self-sustaining combustion like aluminum particles, these processes rely on heat flux propagation, which is limited by factors like phase changes, reaction energies, and product diffusion, and heat transfer during the laser duration. This limitation establishes a maximum penetration distance for effective heating, thereby capping the ignition delay and combustion duration.

Figure 12 indicates that the average combustion duration stabilizes at approximately 800 ms for packs exceeding 4 layers, with a maximum variation of about 10% across different layer counts. This trend indicates that under continuous 200 W laser irradiation for 1.5 s, the thermal penetration depth during the combustion stage is limited to approximately 40 μm. Correspondingly, the flame speed is estimated to be 50 nm/ms. Given that the heat flux during the ignition stage is lower than during combustion—due to the absence of reaction exothermicity—the corresponding heat penetration distance during ignition is expected to be less than 40 μm. This further implies that the average ignition delay should also approach a maximum once the number of layers exceeds 4, a conclusion supported by

the experimental observation. A comparison reveals that while the dispersion in average ignition delay decreases beyond 4 layers (with an upper limit of 82 ms), its maximum deviation across different layer counts exceeds 30%, which is significantly greater than that for combustion duration. The primary reason for this increased uncertainty is the relatively large particle size used in the ignition delay measurements. Since the average ignition delay recorded is about one-eighth of the average combustion duration, the particle size for the delay tests should theoretically be one-eighth of that for the combustion time tests to attain commensurate precision. Hence, applying the same particle size for both measurements, as in this study, results in poorer convergence for the ignition delay data due to this fundamental scaling rationale.

4.2. Results for Unsieved Powders

Premised on the theoretical prediction that a narrow PSD enhances combustion reproducibility, our experiments confirm that the spectral consistency and temporal stability of sieved particles are markedly superior to those of the raw particles. We investigated the combustion dynamics of single-layer raw particles, and the acquired emission spectra are presented in Figure 13.

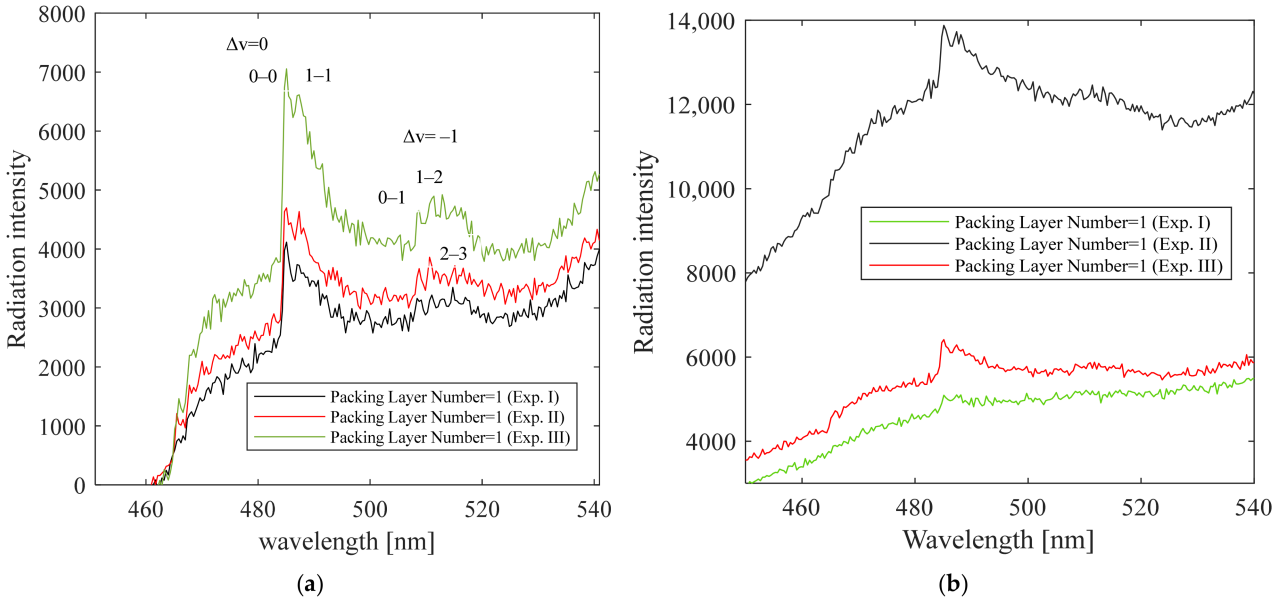


Figure 13. For particles before sieving, spectral profiles of the AlO radical emission band (464.4–513.3 nm) recorded at (**a**) 9 ms and (**b**) 540 ms and without intensity correction, where Δv denotes the net change in the vibrational quantum number, while the v′–v″ notation indicates a specific vibronic transition between defined vibrational energy levels. Results from three independent experimental trials for samples with 1 packing layer.

As shown in Figure 13a, the spectral profiles at 9 ms post-ignition exhibit high conformity in peak positions, yet significant discrepancies arise in absolute intensity and fine structure, accompanied by a lower signal-to-noise ratio (SNR) relative to sieved samples. Quantitatively, the intensity of the Δv = 0 vibrational band varies by up to 1.75-fold across the three replicates. Furthermore, the Δv = −1band is virtually absent in all trials, while the Δv = +1band is only discernible in a single experiment. By 540 ms (Figure 13b), the spectral divergence intensifies; intensity variations reach ~300%, and one replicate loses virtually all characteristic emission features, indicating a severely quenched combustion event.

Beyond spectral degradation, a broad PSD induces profound stochasticity in the combustion process itself. As summarized in Table 1, the ignition delay remain relatively stable across replicates. However, the combustion process exhibits a pronounced stochasticity,

randomly oscillating between high-intensity (strong) and low-intensity (weak) regimes. We attribute this bifurcation primarily to the presence of outlier particles—both significantly smaller and larger than the mode diameter—within the unsieved raw powder. These outliers possess vastly disparate reactivities: ultrafine particles ignite prematurely, acting as erratic hot spots, while coarse particles burn sluggishly, acting as thermal sinks. Consequently, the broad PSD not only degrades the signal-to-noise ratio (SNR) of emission spectra but fundamentally undermines the determinism of the combustion sequence. Therefore, unsieved powders are unsuitable for investigations targeting experimental reproducibility, as their inherent polydispersity convolutes the effects of packing structure with uncontrolled kinetic variances.

Table 1. Ignition delay and combustion duration for unsieved Al particles.

Packing Layers	Ignition Delay (ms)	Strong Combustion Duration (Radiation Intensity Belongs to 2000~4000) (ms)	Weak Combustion Duration (Radiation Intensity Belongs to 500~2000) (ms)
1	9	32	—
1	9	—	110, 190, 270
1	9	250	130

5. Discussion

We investigate the dominant factors governing combustion reproducibility through the lens of reaction interface geometry. While the combustion of particulate ensembles involves intricate, coupled processes—including heat and mass transfer, phase transitions, species diffusion, and heterogeneous chemical kinetics—performing full-physics, high-fidelity simulations across the entire system remains computationally intractable. To address this, we bypass the need to resolve every microscopic combustion detail, instead adopting a simplified theoretical framework to identify the primary drivers of experimental irreproducibility, with subsequent statistical validation against experimental measurements.

Combustion fundamentally manifests as the propagation of a reaction interface through the packed bed. Consequently, the topographical consistency of this interface is hypothesized to be a principal determinant of experimental reproducibility. Localized curvature or corrugation of the reaction front induces heterogeneous burn rates, which can generate anomalous spectral signatures and amplify microscopic non-uniformities through coupled heat- and mass-transfer feedback. In this study, the reaction front is driven by continuous laser irradiation. The nanoscale optical absorption depth in aluminum [19] localizes the initial optical energy deposition at exposed particle surfaces, making the geometry of the nascent reaction front sensitive to the pre-combustion surface topography. During subsequent reaction-interface propagation, heterogeneities in interstitial pore geometry modulate oxidizer transport, product evacuation, and energy dissipation. Variations in pore-throat size alter diffusional path lengths for oxidizer access to particle surfaces, while spatial variations in porosity produce non-uniform local heat dissipation. These coupled gradients in equivalence ratio and thermal energy can undermine spatially uniform combustion and further deform the reaction interface.

Accordingly, this study systematically evaluates two dominant geometric drivers of reaction interface geometrical consistency: surface topography and pore characteristics before combustion. By quantitatively correlating these geometric parameters—derived from DEM simulations—with experimental spectral and temporal signatures, we aim to disentangle their respective contributions to combustion irreproducibility. DEM simulations confirm that the particulate ensemble consistently achieves a dense random-close-packed state. Consequently, the total pore volume is unlikely to be the primary determinant of combustion irreproducibility.

Instead, the heterogeneity of the pore architecture must be analyzed in depth. To achieve this, the 3D pore space was discretized into a high-resolution voxel-based model, within which individual pore bodies were segmented based on pore-throat constrictions. Quantitative analysis revealed substantial variations in pore volume and shape across the bed. As illustrated in Figure 14, three representative pore structures—randomly sampled from the simulation domain—exhibit complex, scaffold-like geometries rather than the quasi-rhombic shapes predicted by simplified 2D calculations.

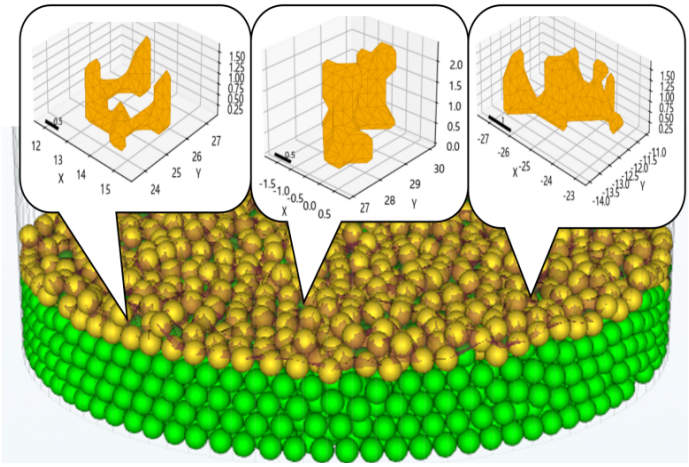


Figure 14. Representative pore architectures extracted from three random locations within the 3D large−scale packed bed. The surface particles are highlighted in yellow, while the others are green.

Pore geometry is inherently complex and cannot be adequately characterized by a single scalar metric. Drawing on established morphometric principles, we use five descriptors: (1) pore volume; (2) principal-axis ratio b/a; (3) principal-axis ratio c/a [33]; (4) pore sphericity [34]; and (5) the pore bounding-box filling ratio f_bb [35]. Here, a, b, and c denote the long, intermediate, and short axes of the best-fit ellipsoid, respectively. The axial ratios b/a and c/a quantify anisotropy and three-dimensional aspect. Values approaching unity indicate isotropic or near-spherical morphologies, whereas lower values indicate elongated or flattened structures. Pore sphericity measures deviation from an ideal sphere and decreases as surface roughness, curvature, or branching increases. Because neither sphericity nor axial ratios fully represent sparse or branched occupancy within an external envelope, f_bb is defined as the pore-body volume divided by the volume of its axis-aligned bounding box. Values approaching unity indicate compact occupancy, whereas lower values indicate sparse, tortuous, or highly branched structures within the box.

The evolution of pore characteristics with packing layer count in the 3D large-scale simulation is presented in Figure 15. The consistency of pore volume and pore shape metrics exhibits a variation of less than 20% across increasing layers—a trend far less sensitive than that observed for surface topography. Crucially, the simulated surface topography similarity aligns favorably with experimental measurements in both trend and magnitude. Experimental data (Figure 10) reveal an optimal consistency of 0.9 for a monolayer, decreasing slightly to 0.82 for bilayers, followed by a precipitous drop to 0.4 for trilayers, with values remaining below 0.4 thereafter. This behavior is faithfully reproduced by the simulations: Speaks at 0.94 for a monolayer, reduces to 0.48 for bilayers, and collapses to 0.25 for trilayers, stabilizing at this lower level. For the bilayer configuration, the calculated similarity is substantially lower than the experimentally measured FWHM consistency. This discrepancy may stem from finite-size limitations in the 3D simulations. Furthermore, it is important to recognize that geometric similarity and spectral consistency may be not strictly linearly correlated metrics; S only captures the static boundary condition,

whereas FWHM integrates complex, non-linear convolution effects of temperature, species concentration, and radiative transfer, potentially decoupling the two measures. While the absolute consistency values for pore metrics remain high (>80%), their evolutionary trends partially mirror experimental observations. Pore volume consistency is highest for monolayers (0.99) and bilayers (0.94), decreases to 0.84 at three layers, and subsequently declines gradually—matching the experimental trajectory. Similarly, the principal axis ratios (b/a and c/a) maintain high consistency at monolayers (0.98 and 0.97, respectively), decrease marginally at bilayers (0.91 and 0.87), and stabilize thereafter. The primary deviation from experimental data occurs specifically at the bilayer condition. Conversely, the bounding box filling ratio and sphericity exhibit near-invariant consistency (~98%) regardless of layer count. We therefore conclude that these latter two metrics exert a negligible influence on combustion reproducibility.

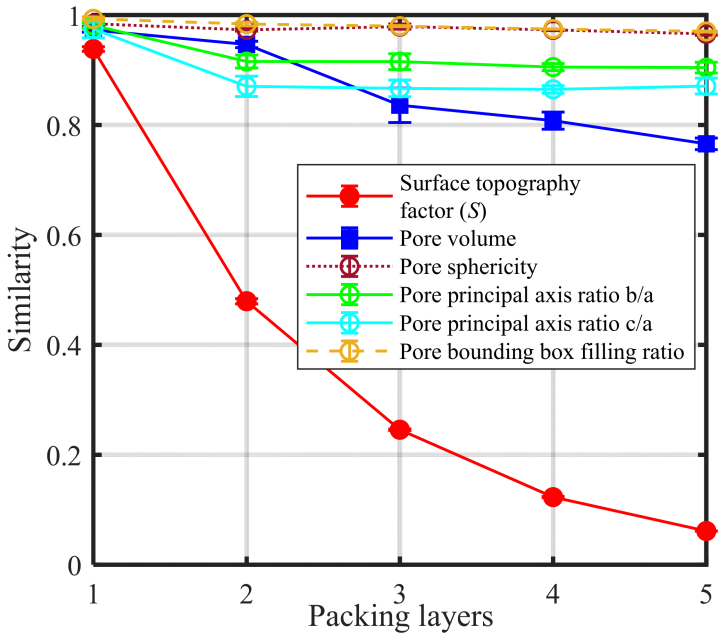


Figure 15. Evolution of surface topography and pore structure metrics with packing layer count in 3D large-scale simulations.

Consequently, we posit that for laser-irradiated micron-sized Al particles, the geometry of the reaction interface is primarily dictated by the pre-combustion surface topography of the uppermost packing layer. In multilayer densely packed ensembles, the constrained translational degrees of freedom of constituent particles enforce geometric continuity across adjacent layers. So the dominant topographical features of the surface-defined initial reaction interface are passively inherited by underlying layers during initial propagation. During reaction propagation, secondary modulation of the reaction front arises from two quantifiable pore metrics: total pore volume and the principal axis aspect ratio of individual pore bodies. In contrast, we argue that the factor of pore sphericity and pore bounding box filling ratio exert negligible effects, as schematically illustrated in Figure 16. Published studies support a measurable link between particle-scale organization and reaction-front structure. In composite propellants, Isert et al. [36] showed that the oxidizer coarse-to-fine ratio changes the microscale flame structure, directly linking formulation-scale particle geometry to the flame field. In aluminum powder beds, Nazarenko et al. [37] distinguished surface and in-depth flame-propagation modes, demonstrating that packed-bed structure influences reaction-front development.

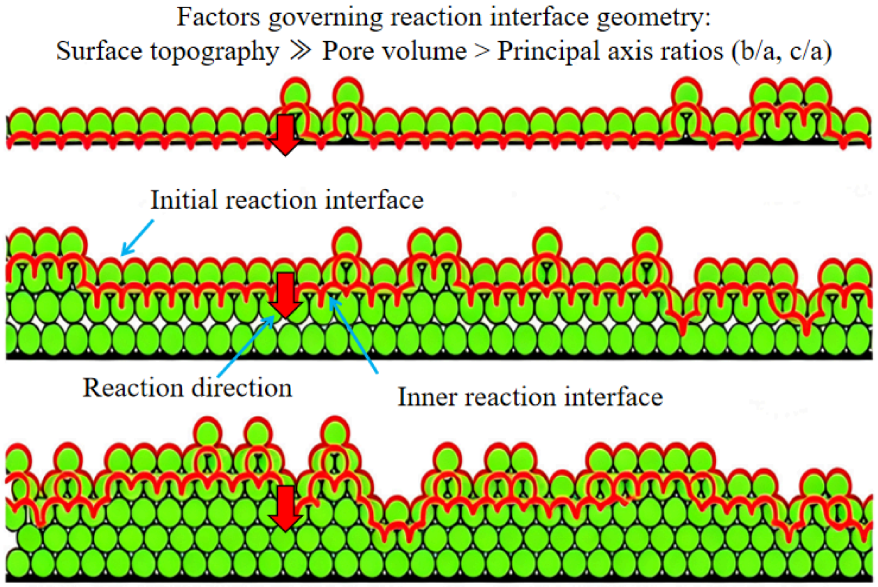


Figure 16. Key factors influencing reaction interface geometry.

Critically, we hypothesize that inter-sample heterogeneity in pore architecture originates predominantly from variations in surface topography. The DEM simulations confirm that the particulate ensemble consistently achieves a dense random-close-packed state, where total pore volume is tightly constrained. If pre-combustion surface topography is invariant across samples, the geometric arrangement of the entire particulate ensemble, and correspondingly the interconnected 3D pore network, will be statistically indistinguishable. This hierarchical coupling explains why surface topography serves as the root driver of combustion reproducibility in the present system. All the above factors are passive byproducts of the dense random-close-packed configuration, rather than active regulators of reaction or transport kinetics. A quantitative investigation into their residual influence is deferred to future work.

6. Conclusions

This work resolves the long-standing challenge of poor experimental reproducibility in laser-ignited particulate combustion via an integrated computational–experimental framework. Key conclusions are as follows:

1. 3D DEM simulations reveal that increasing packing layers causes a monotonic decay in surface topography conformity, while bulk packing density remains near its theoretical maximum due to gravitational settling—contradicting the classical assumption that density variations dominate irreproducibility.
2. Integrating multistage sieving, ECPC theory, and controlled droplet deposition, the constrained droplet method fabricates programmable multilayer packings with narrow PSD that match computational model inputs. Pre-sieving is validated as critical for eliminating particle-size-induced run-to-run variability in combustion performance.
3. In situ laser ignition diagnostics show that the consistency of AlO spectral features, ignition delay, and combustion duration decays sharply for $\geq$3 packing layers, quantitatively matching the simulated decline in surface topography conformity. Pore volume and principal axis ratios exert secondary effects, while pore sphericity and compactness have negligible influence.

Mechanistically, the surface topography of the uppermost layer dictates the initial reaction interface geometry, which is propagated to underlying layers via the tight packing

structure. This work reveals the controlling factor of laser-ignited combustion in random packings and provides a standardized protocol for reproducible sample preparation.

Author Contributions: Conceptualization, X.L.; Methodology, X.L., S.L. and M.H.; Software, Z.Z.; Validation, S.L.; Formal analysis, M.H.; Investigation, X.L., Q.L. and F.L.; Resources, X.L., Q.L., W.G. and H.P.; Data curation, H.P.; Writing—original draft, S.L.; Writing—review & editing, X.L. and S.L.; Visualization, S.L.; Supervision, F.L. and W.G.; Project administration, W.G.; Funding acquisition, H.P. and X.L. All authors have read and agreed to the published version of the manuscript.

Funding: The work was supported by the National Key Laboratory of Shock Wave and Detonation Physics (Grant No. 2024CXPTGFJJ06408), National Natural Science Foundation of China (Grant No. 11902276); National Key Laboratory of Computational Physics (Grant No. JK2025-04); Fundamental Research Funds for the Central Universities (Grant No.2682025ZTPY002).

Data Availability Statement: The original contributions presented in this study are included in the article. Further inquiries can be directed to the corresponding author.

Acknowledgments: The authors are grateful for the language polishing supported by Artificial Intelligence YuanBao (Version 4 August 2026; Hunyuan model).

Conflicts of Interest: The authors declare that they have no known competing financial interests or personal relationships that could have appeared to influence the work reported in this paper.

References

1. Bai, Y.; Chen, H.; Wu, X.; Yang, W.; Zhu, F.; Chu, K.; Ba, Y. Euler-Lagrange simulation of massive aluminum particles and agglomerates combustion in a realistic solid rocket motor environment. *Powder Technol.* **2026**, *468*, 121685. [CrossRef]
2. Peng, F.; Liu, H.; Cai, W. Combustion diagnostics of metal particles: A review. *Meas. Sci. Technol.* **2023**, *34*, 042002. [CrossRef]
3. Hu, Z.; Feng, Y.; Dong, W.; Tang, Y.; Li, J.; Liao, L.; Zhao, M.; Shi, B. Comprehensive modeling of ignition and combustion of multiscale aluminum particles under various pressure conditions. *Chin. J. Aeronaut.* **2024**, *37*, 188–202. [CrossRef]
4. Beckstead, M.W.; Newbold, B.R. A summary of aluminum combustion. In *RTO/VKI Special Course on Internal Aerodynamics in Solid Rocket Propulsion*; NATO Research and Technology Organisation: Brussels, Belgium; von Karman Institute for Fluid Dynamics: Sint-Genesius-Rode, Belgium, 2004.
5. De Lucia, F.C., Jr.; Dean, S.W.; Gottfried, J.L. Commercial aluminum powders, part II: Energy release rates induced by rapid heating via pulsed laser excitation. *Powder Technol.* **2022**, *399*, 117161. [CrossRef]
6. Felber, C.; Köberl, M.; Jägle, E.A. Powder bed fusion—Laser beam in reactive atmospheres—Ignition limits for Fe and Ti-6Al-4V powder blends in CO_2 and N_2. *Powder Technol.* **2025**, *456*, 120843. [CrossRef]
7. Zhu, S.; Huang, Y.; Li, L.; Wei, X.; Liu, B. Research on laser induced plasma ignition of gas oxygen/methane. *Acta Astronaut.* **2024**, *217*, 208–220. [CrossRef]
8. Zhakeyev, A.; Wang, P.; Zhang, L.; Shu, W.; Wang, H.; Xuan, J. Additive manufacturing: Unlocking the evolution of energy materials. *Adv. Sci.* **2017**, *4*, 1700187. [CrossRef] [PubMed]
9. Endraß, S.M.J.; Klapötke, T.M.; Lechner, J.T.; Stierstorfer, J. Application of 1- and 2-propargyl-tetrazole in laser-ignitable energetic coordination compounds. *FirePhysChem* **2023**, *3*, 330–338. [CrossRef]
10. Kamaraj, N.; Ghoroi, C.; Sundaram, D.S. Influence of particle size and packing density on combustion of compacted nickel-aluminum powder mixtures. *Combust. Sci. Technol.* **2025**, *197*, 6552–6579. [CrossRef]
11. Averardi, A.; Cola, C.; Zeltmann, S.E.; Gupta, N. Effect of particle size distribution on the packing of powder beds: A critical discussion relevant to additive manufacturing. *Mater. Today Commun.* **2020**, *24*, 100964. [CrossRef]
12. Yan, N.; Zeng, Y.-Q.; Fu, H. Relationship between laser ignition delay time and charge density of of $Zr/KClO_4$. *Chin. J. Energ. Mater.* **2008**, *5*, 487–489.
13. Saceleanu, F.; Idir, M.; Chaumeix, N.; Wen, J.Z. Combustion characteristics of physically mixed 40 nm aluminum/copper oxide nanothermites using laser ignition. *Front. Chem.* **2018**, *6*, 465. [CrossRef] [PubMed]
14. Pantoya, M.L.; Levitas, V.I.; Granier, J.J.; Henderson, J.B. Effect of bulk density on reaction propagation in nanothermites and micron thermites. *J. Propuls. Power* **2009**, *25*, 465–470. [CrossRef]
15. Bharat, N.T.; Mishra, D.P. The effect of disorderness in 2D adiabatic heterogeneous solid combustion under unstable and quenching regimes. *Combust. Theory Model.* **2025**, *29*, 541–568. [CrossRef]
16. Sundaram, D.S.; Yang, V. Effect of packing density on flame propagation of nickel-coated aluminum particles. *Combust. Flame* **2014**, *161*, 2916–2923. [CrossRef]

17. Sullivan, K.T.; Piekiel, N.W.; Wu, C.; Chowdhury, S.; Kelly, S.T.; Hufnagel, T.C.; Fezzaa, K.; Zachariah, M.R. Reactive sintering: An important component in the combustion of nanocomposite thermites. *Combust. Flame* **2012**, *159*, 2–15. [CrossRef]
18. Stacy, S.C.; Pantoya, M.L. Laser ignition of nano-composite energetic loose powders, Propellants, Explosives. *Pyrotechnics* **2013**, *38*, 441–447. [CrossRef]
19. Rakić, A.D. Algorithm for the determination of intrinsic optical constants of metal films: Application to aluminum. *Appl. Opt.* **1995**, *34*, 4755–4767. [CrossRef] [PubMed]
20. Kruggel-Emden, H.; Sturm, M.; Wirtz, S.; Scherer, V. Selection of an appropriate time integration scheme for the discrete element method (DEM). *Comput. Chem. Eng.* **2008**, *32*, 2263–2279. [CrossRef]
21. Efrat, A.; Fan, Q.; Venkatasubramanian, S. Curve matching, time warping, and light fields: New algorithms for computing similarity between curves. *J. Math. Imaging Vis.* **2007**, *27*, 203–216. [CrossRef]
22. Meier, C.; Weissbach, R.; Weinberg, J.; Wall, W.A.; Hart, A.J. Critical influences of particle size and adhesion on the powder layer uniformity in metal additive manufacturing. *J. Mater. Process. Technol.* **2019**, *266*, 484–501. [CrossRef]
23. Besl, P.J.; McKay, N.D. A method for registration of 3-D shapes. *IEEE Trans. Pattern Anal. Mach. Intell.* **1992**, *14*, 239–256. [CrossRef]
24. Huttenlocher, D.P.; Klanderman, G.A.; Rucklidge, W.J. Comparing images using the Hausdorff distance. *IEEE Trans. Pattern Anal. Mach. Intell.* **1993**, *15*, 850–863. [CrossRef]
25. He, K.; Ye, H.; Wang, Z.; Liu, J. An efficient quasi-physical quasi-human algorithm for packing equal circles in a circular container. *Comput. Oper. Res.* **2018**, *92*, 26–36. [CrossRef]
26. Frizzo, C.P.; Vieira, J.C.B.; Krüger, N.; Paz, A.V.; Zanatta, N.; Villetti, M.A. Heating profile of long alkyl chain ionic liquid doped solvents under ultrasound irradiation. *J. Solut. Chem.* **2021**, *50*, 240–256. [CrossRef]
27. Li, X.-D.; Sun, H.; Yang, Y.; Song, C.-G.; Liu, H.-M.; Wang, J.-Y. Preparation and dispersion stability of spray-drying precursor nano-Al suspension. *Chin. J. Energ. Mater.* **2020**, *28*, 773–778. (In Chinese)
28. Bazyn, T.; Krier, H.; Glumac, N. Evidence for the transition from the diffusion-limit in aluminum particle combustion. *Proc. Combust. Inst.* **2007**, *31*, 2021–2028. [CrossRef]
29. Luo, C.; Yi, Z.; Liu, Q.; Liu, F.; Guo, W.; Pei, H.; Li, X. Investigating the interaction mechanisms of aluminum particles in laser-induced ignition experiments. *Propellants Explos. Pyrotech.* **2025**, *50*, e12030. [CrossRef]
30. Peng, Z.; Yang, Q.; Li, C.; Zhu, N.; Jiang, Z. Investigation on spectra of the B2Σ+-X2Σ+ and C2Πr-X2Σ+ bands of AlO radicals in a shock tube. *Spectrosc. Spectr. Anal.* **2010**, *30*, 865–868. (In Chinese) [CrossRef]
31. Cremers, D.A.; Radziemski, L.J. *Handbook of Laser-Induced Breakdown Spectroscopy*, 2nd ed.; Wiley: Chichester, UK, 2013.
32. Badiola, C.; Gill, R.J.; Dreizin, E.L. Combustion characteristics of micron-sized aluminum particles in oxygenated environments. *Combust. Flame* **2011**, *158*, 2064–2070. [CrossRef]
33. Blott, S.J.; Pye, K. Particle shape: A review and new methods of characterization and classification. *Sedimentology* **2008**, *55*, 31–63. [CrossRef]
34. Wadell, H. Volume, shape, and roundness of quartz particles. *J. Geol.* **1935**, *43*, 250–280. [CrossRef]
35. Rosin, P.L. Measuring shape: Ellipticity, rectangularity, and triangularity. *Mach. Vis. Appl.* **2003**, *14*, 172–184. [CrossRef]
36. Isert, S.; Hedman, T.D.; Lucht, R.P.; Son, S.F. Oxidizer coarse-to-fine ratio effect on microscale flame structure in a bimodal composite propellant. *Combust. Flame* **2016**, *163*, 406–413. [CrossRef]
37. Nazarenko, O.B.; Sechin, A.I.; Sechin, A.A.; Amelkovich, Y.A. Flame propagation behavior of aluminum nanopowder in bulk layer. *J. Loss Prev. Process Ind.* **2021**, *69*, 104353. [CrossRef]

Disclaimer/Publisher's Note: The statements, opinions and data contained in all publications are solely those of the individual author(s) and contributor(s) and not of MDPI and/or the editor(s). MDPI and/or the editor(s) disclaim responsibility for any injury to people or property resulting from any ideas, methods, instructions or products referred to in the content.